

Applicability of the Rayleigh-Gans approximation for scattering by snowflakes at microwave frequencies in vertical incidence

J. Tyynelä,¹ J. Leinonen,^{2,3} C. D. Westbrook,⁴ D. Moiseev,¹ and T. Nousiainen¹

Received 11 May 2012; revised 4 January 2013; accepted 4 January 2013; published 25 February 2013.

[1] The applicability of the Rayleigh-Gans approximation (RGA) for scattering by snowflakes is studied in the microwave region of the electromagnetic spectrum. Both the shapes of the single ice crystals, or monomers, and their amounts in the modeled snowflakes are varied. For reference, the discrete-dipole approximation (DDA) is used to produce numerically accurate solutions to the single-scattering properties, such as the backscattering and extinction cross-sections, single-scattering albedo, and the asymmetry parameter. We find that the single-scattering albedo is the most accurate with only about 10% relative bias at maximum. The asymmetry parameter has about 0.12 absolute bias at maximum. The backscattering and extinction cross-sections show about –65% relative biases at maximum, corresponding to about –4.6 dB difference. Overall, the RGA agrees well with the DDA computations for all the cases studied and is more accurate for the integrated quantities, such as the single-scattering albedo and the asymmetry parameter than the cross-sections for the same snowflakes. The accuracy of the RGA seems to improve, when the number of monomers is increased in an aggregate, and decrease, when the frequency increases. It is also more accurate for less dense monomer shapes, such as stellar dendrites. The DDA and RGA results are well correlated; the sample correlation coefficients of those are close to unity throughout the study. Therefore, the accuracy of the RGA could be improved by applying appropriate correction factors.

Citation: Tyynelä, J., J. Leinonen, C. D. Westbrook, D. Moiseev, and T. Nousiainen (2013), Applicability of the Rayleigh-Gans approximation for scattering by snowflakes at microwave frequencies in vertical incidence, *J. Geophys. Res. Atmos.*, 118, 1826–1839, doi:10.1002/jgrd.50167.

1. Introduction

[2] Space- and ground-based snowfall measurements are necessary when monitoring the impact of winter-type precipitation on the environment in local and global scale. With the presence of radars and passive radiometers onboard satellites, such as NASA's Global Precipitation Measurement, CloudSat, and Aqua missions, and ESA's Earth-CARE, there is a demand to know how snowflakes scatter microwave radiation. Due to the large morphological variance of snowflakes, it is also crucial that the computational methods are accurate and efficient in order for them to be operationally useful. There has already been systematic forward modeling at microwave frequencies for single ice crystals by Liu [2008] and Hong *et al.* [2009], but not for aggregates of ice crystals due to the many free parameters in such shape models.

[3] The retrieval of snow microphysical parameters from backscattered signals is an ill-conditioned inverse problem. To reduce the number of unknowns, assumptions are needed. Forward scattering modeling can be a valuable aid in choosing the assumptions made. To this end, it is important to have a reliable forward model for the assessment of the impact of different physical properties of snowflakes on scattering. Ideally, such a model should also be conceptually simple and computationally inexpensive.

[4] Accurate computations can be obtained using the discrete-dipole approximation [Purcell and Pennypacker, 1973] or other methods that are applicable for arbitrarily shaped scatterers. Although these methods can be expected to give reliable results, they are computationally expensive. The traditional approach has been to simplify the shapes of the snowflakes, modeling them as spheres or spheroids [e.g., Bohren and Battan, 1980; Hogan *et al.*, 2000; Korolev and Isaac, 2003; Matrosov, 2007; Austin *et al.*, 2009] and compute the scattering properties using the exact numerical methods available for such shapes. For spheres, the Mie solution [Mie, 1908] is used; for spheroids, the *T*-matrix method [Waterman, 1965] is commonly applied. However, it has been recognized recently that for snowflakes larger than the wavelength, the backscattering cross-sections given by these shape models can introduce an absolute error as high as orders of

¹Department of Physics, University of Helsinki, Helsinki, Finland.

²Finnish Meteorological Institute, Helsinki, Finland.

³Department of Applied Physics, Aalto University, Espoo, Finland.

⁴Department of Meteorology, University of Reading, Berkshire, UK.

Corresponding author: J. Tyynelä, Department of Physics, PO Box 48, FI-00014, University of Helsinki, Helsinki, Finland. (jktynel@mappi.helsinki.fi)

©2013. American Geophysical Union. All Rights Reserved.
2169-897X/13/10.1002/jgrd.50167

magnitude [Ishimoto, 2008; Botta et al., 2010; Petty and Huang, 2010; Tyynelä et al., 2011].

[5] An alternative approach is to simplify the physics of the scattering theory instead of the target shape. One such theory is the Rayleigh-Gans approximation [Bohren and Huffman, 1983]. The RGA neglects the higher-order interactions of electromagnetic radiation within the particle, considerably simplifying the mathematics of the problem. In RGA, the scattered wave from the whole particle is simply a superposition of the scattered waves originating from different parts of the particle; the interactions between the parts are ignored. This allows the scattering matrix to be determined from a straightforward integration over the particle volume. When the snowflake is represented as a volumetric model composed of small volume elements (such as the dipoles in the DDA), the integral is fast and straightforward to calculate numerically. Another potential benefit is that the simple formula of the Rayleigh-Gans integral allows one to study the scattering properties analytically, providing a tool to connect microphysics and scattering properties.

[6] The Rayleigh-Gans theory has been recognized to be suitable for computing scattering from fractal aggregates [Berry and Percival, 1986] and has been previously applied to snowflakes on theoretical grounds [Matrosov, 1992; Westbrook et al., 2006; Hogan et al., 2012]. However, no comprehensive validation of the applicability of the RGA on realistically shaped snowflakes has been performed. In this paper, we perform such a validation by comparing the results of the RGA and DDA computations for aggregate snowflakes of different ice crystal types generated with a physically based model. We have chosen nine frequencies from the range that is the most relevant for cloud and precipitation remote sensing: 3, 14, 36, 60, 90, 120, 150, 180, and 220 GHz. For the refractive indices of water ice at different frequencies, we use the formulas by Jiang and Wu [2004].

2. Numerical Methods

2.1. Shape Models for Snowflakes

[7] In order to use realistic snowflake models in the computations, a physically based aggregation model for single ice crystals is applied [Westbrook, 2004]. We also simulate the horizontal alignment of falling snowflakes in a simple way by reorienting the particles based on their principal axes of inertia tensor after each aggregation event. Due to the lack of observations, the orientation of the individual crystal in an aggregate is assumed to be random due to the complex flow around the snowflakes and ice crystals.

[8] To explore variability in the crystals shapes, we use four common crystal types in the study: stellar dendrites, thin and thick hexagonal plates, hexagonal columns, and six-bullet rosettes. One goal is to establish how the shape of the monomers in an aggregate affects the applicability of the RGA. For the stellar dendrites, we use the crystal growth algorithm by Reiter [2005]. The diameter-to-thickness ratio is fixed at 100 for both the stellar dendrites and the thin hexagonal plates. For the hexagonal columns, the length-to-thickness ratio is fixed at 10. For the thick hexagonal plates, the diameter-to-thickness ratio is also fixed at 10. These values correspond to the more extreme cases reported by Takahashi et al. [1991], but are used to get the maximum variability between shapes. For the bullet rosettes, we use

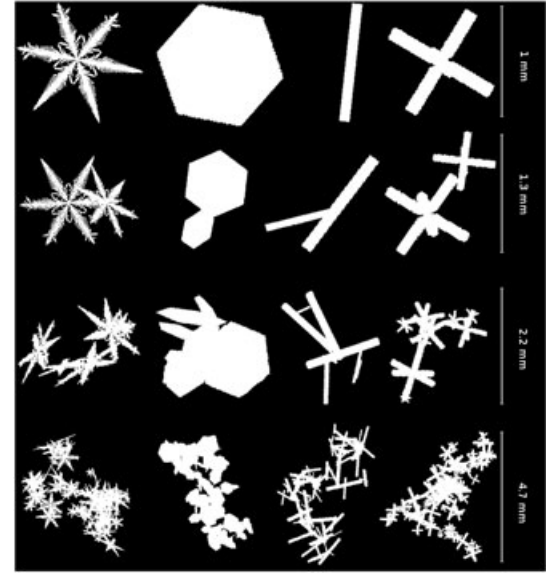


Figure 1. Examples of the modeled snowflakes as viewed from the incident direction. From the top to the bottom row, the number of crystals are 1, 2, 10, and 100. From the left to the right column, the shapes of crystals are stellar dendrite, thin hexagonal plate, hexagonal column, and six-bullet rosette. The average sizes for a given number of crystals are shown on the right side.

symmetric six-bullet rosettes with the shapes of individual bullets adopted from Um and McFarquhar [2007].

[9] We have chosen four different sizes of aggregates based on the number of ice crystals in them: 1, 2, 10, and 100. Regardless of the crystal type, the monomer diameters vary according to the probability density function [Mitchell, 1991]

$$P(D) = \Lambda \exp(-\Lambda D_{\max}), \quad (1)$$

where $\Lambda = 1 \text{ mm}^{-1}$ and D_{\max} is the maximum diameter in millimeters. The diameter is truncated at 0.5 mm in the lower end of the distribution, because aggregation is not very efficient for small ice crystals [Pruppacher and Klett, 1997]. The diameter is also truncated at 2.0 mm in the higher end of the distribution, because larger ice crystals are not that common for all shapes. The average diameter of the monomers is fixed to 1 mm. In Figure 1, sample images of the aggregates are presented. For each aggregate type and size, we produce 50 random sample particles. In this study, our primary interest has not been to closely mimic any specific snowflake type, but rather to cover a wide parameter range of naturally occurring snowflakes to more comprehensively test the RGA approach.

2.2. Single-Scattering Properties

[10] When computing the single-scattering properties, we have adopted the conventions of Bohren and Huffman [1983]. The relation between the incident and scattered electric fields (\mathbf{E}_{inc} and \mathbf{E}_{sca} , respectively) is given by the amplitude scattering matrix:

$$\begin{pmatrix} E_{\text{sca},\parallel} \\ E_{\text{sca},\perp} \end{pmatrix} = \frac{e^{ik(r-z)}}{-ikr} \begin{pmatrix} S_2 & S_3 \\ S_4 & S_1 \end{pmatrix} \begin{pmatrix} E_{\text{inc},\parallel} \\ E_{\text{inc},\perp} \end{pmatrix}, \quad (2)$$

where the symbols \parallel and \perp denote the electric-field components parallel and perpendicular to the scattering plane, respectively, k is the wave number, and r is the radial distance. The elements of the amplitude scattering matrix are functions of shape, size parameter, refractive index, and orientation of the scatterer. The elements also depend on the scattering direction specified by the scattering angle θ and the azimuth angle ϕ . For spherical particles, the S_3 and S_4 elements of the amplitude scattering matrix are zero due to the symmetry in shape. They are also zero for the RGA regardless of particle shape due to the simplified scattering theory. This is generally not true for irregular particles or symmetric non-spherical particles with preferential orientations. The formulas presented in the latter part of this section are valid for the Mie theory and the RGA.

[11] The horizontal backscattering cross-section

$$\sigma_{\text{hh}} = \frac{4\pi}{k^2} |S_1(180^\circ, 0^\circ)|^2 \quad (3)$$

relates the incident irradiance to the backscattered power at horizontal polarization. It is proportional to the radar reflectivity. For all the other single-scattering properties considered here, the incident wave is unpolarized. Thus, the properties must be averaged over two mutually perpendicular incident polarizations.

[12] The absorption cross-section is given by

$$\sigma_{\text{abs}} = \frac{1}{2} (\sigma_{\text{abs},X} + \sigma_{\text{abs},Y}) = \frac{2\pi}{k^2} \text{Re} [S_2(0^\circ, 0^\circ) + S_1(0^\circ, 0^\circ)], \quad (4)$$

where the subscripts X and Y denote the direction of the incident polarization. It specifies how much of the incident irradiance is absorbed by the scatterer. The formulas are derived from the optical theorem [van de Hulst, 1957].

[13] The scattering cross-section

$$\sigma_{\text{sca}} = \frac{1}{2} (\sigma_{\text{sca},X} + \sigma_{\text{sca},Y}) = \frac{1}{2k^2} \int_0^{2\pi} \int_0^\pi (|S_2|^2 + |S_1|^2) \sin \theta \, d\theta \, d\phi \quad (5)$$

relates the incident irradiance to the scattered power in all directions.

[14] The extinction cross-section

$$\sigma_{\text{ext}} = \sigma_{\text{abs}} + \sigma_{\text{sca}} \quad (6)$$

measures the total scattered and absorbed power in all directions by the particle. It can also be derived from (4), if the radiation reaction correction is used for $S_{1,2}(0^\circ, 0^\circ)$ [van de Hulst, 1957]. The extinction cross-section is related to the attenuation of the radar signal in the atmosphere.

[15] The single scattering albedo

$$\varpi = \frac{\sigma_{\text{sca}}}{\sigma_{\text{ext}}} \quad (7)$$

is a measure of the relative contribution of scattering and absorption by the particle in all directions.

[16] The asymmetry parameter

$$g = \frac{1}{2k^2 \sigma_{\text{sca}}} \int_0^{2\pi} \int_0^\pi (|S_2|^2 + |S_1|^2) \cos \theta \sin \theta \, d\theta \, d\phi, \quad (8)$$

describes the relative contribution of the scattered intensity in the forward and backward scattering directions. It is positive if the scattered intensity is directed predominantly

into the forward hemisphere and negative if into the backward hemisphere. Both ϖ and g are important in modeling the multiple scattering of radar signals detected by space-borne cloud radar [Hogan and Battaglia, 2008] and for radiative transfer computations used to interpret the passive microwave measurements.

[17] In the computations, the scattering parameters are averaged over 50 random samples and 5 different horizontal orientations, and vertical incidence is used for all computations similar to many space-borne radars and ground-based cloud radars. The scattering cross-sections and asymmetry parameters are computed using Monte Carlo integration with 1000 random scattering directions. The average ϖ is computed from the ratio of the average scattering and extinction cross-sections.

2.3. Rayleigh-Gans Approximation

[18] In general, solving (2) for an irregularly shaped scatterer is difficult and usually cannot be done analytically. However, such a particle can be divided into small volume elements that can be handled separately. If the size parameter $x = ka$ (a is the radius of the volume element) of the volume elements is small enough, scattering for the individual elements can be solved using the classical Rayleigh approximation. In the far-field, the total scattered wave is a superposition of the scattered waves from each volume element. By integrating over all scattering elements in a particle and neglecting the electromagnetic interactions between them, the single-scattering properties of the whole scatterer can be approximately computed. This is called the Rayleigh-Gans approximation. The resulting amplitude scattering matrix elements are

$$S_1 = -\frac{3i}{4\pi} \frac{m^2 - 1}{m^2 + 2} k^3 V f(\theta, \phi), \quad S_2 = S_1 \cos \theta, \quad S_3 = 0, \quad S_4 = 0, \quad (9)$$

where V is the volume of the particle, m the refractive index, and $f(\theta, \phi)$ the form factor of a homogeneous particle, which gives the deviation from the Rayleigh approximation. It is given by

$$f(\theta, \phi) = \frac{1}{V} \int_V e^{i\delta(\theta, \phi)} dV, \quad \delta(\theta, \phi) = \mathbf{R} \cdot (\mathbf{k}_{\text{inc}} - \mathbf{k}_{\text{sca}}), \quad (10)$$

where $\delta(\theta, \phi)$ is the phase-difference factor between the partial waves in the far-field, \mathbf{k}_{inc} and \mathbf{k}_{sca} are the wave vectors of the incident and scattered waves, respectively, and \mathbf{R} is the position vector of the volume elements. Note that the amplitude matrix elements defined in (9) are identical to the Rayleigh approximation for spherical particles, when $x \ll 1$, because in this case the form factor equals unity in all scattering directions. The form factor also always equals one in the forward scattering direction.

[19] The traditional requirements for the validity of the RGA are that the refractive index of the particle must be close to that of the surrounding medium and that the maximum phase shift of the incident wave through the particle is small. In a mathematical form,

$$|m - 1| \ll 1, \quad 2x|m - 1| \ll 1. \quad (11)$$

The latter requirement suggests that the RGA can be applied to substantially larger particles than the Rayleigh approximation, provided that the former requirement is already

fulfilled. *Berry and Percival* [1986] showed that the former requirement can be significantly relaxed for aggregates due to the large air gaps between the solid parts of the particle. For irregular particles, the requirements mean that the volume elements must be far away from most others so that the induced field is close to the incident field, and that their mutual electromagnetic interactions are therefore diminished and can be ignored. Due to this, we argue that m in (11) is more related to the effective refractive index of the particle that takes into account the fluffiness, rather than the absolute refractive index of the solid matter. As most of the particles in this study have very low densities, we checked the validity of this argument by computing the effective refractive indices for all particles (see section 4). It should be noted that elsewhere in the present study, m is the refractive index of solid ice.

2.4. Discrete-Dipole Approximation

[20] In the previous section, it was assumed that the scatterer can be divided into small independently scattering volume elements. Since it is not evident when it is safe to make such an assumption, it is important to compare the scattered field characteristics to cases where also the mutual interactions are taken into account. For this purpose, the discrete-dipole approximation is a convenient method [*Purcell and Pennypacker*, 1973].

[21] In the DDA, the scatterer is again divided into N small volume elements, dipoles, that are placed into a regular cubic lattice separated by a distance d . The induced dipole moments \mathbf{P}_i ($i = 1, 2, \dots, N$) for each dipole are computed from a set of equations:

$$\mathbf{E}_i^{\text{inc}} = \beta_i^{-1} \mathbf{P}_i + \sum_{j \neq i} \mathbf{G}(\mathbf{r}_i, \mathbf{r}_j) \mathbf{P}_j, j = 1, 2, \dots, N, \quad (12)$$

where $\mathbf{E}_i^{\text{inc}}$ is the incident field at dipole i , $\beta_i(m, k, d)$ the polarizability tensor of dipole i , and \mathbf{G} the Green's tensor between dipoles i and j . For the polarizability of single dipoles, there are several formulas available [*Yurkin and Hoekstra*, 2011]. Once the dipole moments have been computed, the near-field interactions between the dipoles are then included in the scattered waves from the dipoles. This is contrary to RGA, where the interactions are neglected. As was discussed in the previous section, less dense particles tend to have more air gaps and the dipoles are more separated, which means that the induced dipole moments are mainly the result of the incident wave (first term on the right side of equation (12)). In this sense, the RGA is the low-density limit of the DDA.

[22] To solve (12) numerically, we use the ADDA program by *Yurkin and Hoekstra* [2011]. In the DDA computations, we use the filtered coupled dipoles, which are generally the most accurate of the choices available for the polarizability [*Yurkin et al.*, 2010]. For the validity of the DDA, it is usually required that the shape is adequately represented by the distribution of dipoles and that $|m|kd < 0.5$ [*Penttilä et al.*, 2007]. In our computations, $|m|kd$ is at maximum 0.41 for all shapes and frequencies. For different monomer shapes and numbers of monomers in an aggregate, it varies. The number of dipoles in a single crystal has

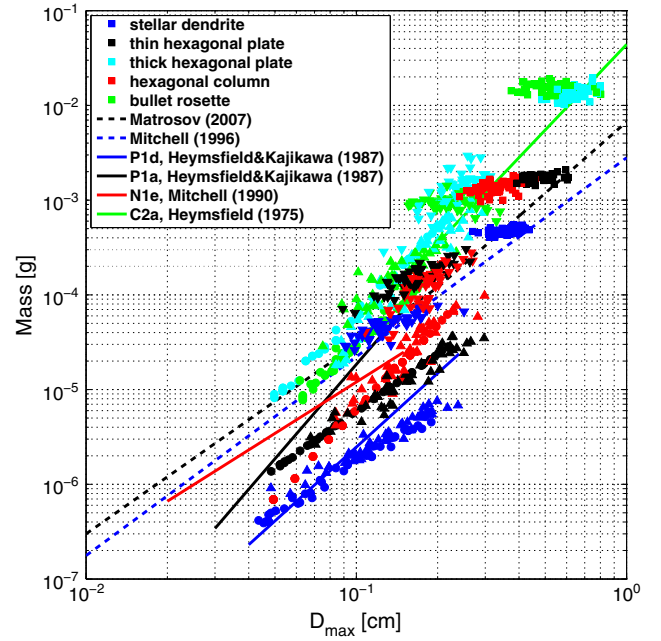


Figure 2. The mass of the snowflakes as a function of the maximum diameter. The modeled particles are shown with different symbols and colors: dots for single crystals, upper triangles for two-monomer aggregates, lower triangles for 10-monomer aggregates, and squares for 100-monomer aggregates. Stellar dendrites are shown in blue, thin hexagonal plates in black, thick hexagonal plates in cyan, hexagonal columns in red, and six-bullet rosettes in green. We also show the empirical mass-diameter relationship in solid lines using the same color coding for the corresponding ice crystal types according to the classification of *Magono and Lee* [1966]. The m - D relationships for all types of snow by *Mitchell* [1996] and *Matrosov* [2007] are shown in dashed lines.

been chosen to be large enough to adequately represent the shape, but small enough that the largest aggregates can still be computed in a reasonable amount of CPU time. The same volume-element subdivision is used for both the RGA and the DDA.

[23] Even though DDA is an accurate tool to compute scattering from arbitrary-shaped particles, it must be validated with other methods. For simpler shapes, it compares favorably with exact numerical methods and scattering theories, such as the Mie theory and null-field method with discrete sources [*Wriedt and Comberg*, 1998; *Yurkin and Hoekstra*, 2011]. For more irregular shapes, such as snowflakes, it can be verified in a laboratory experiment using microwave analog measurements [*Vaillon et al.*, 2011]. Previously, forward-scattering properties of single snowflakes have been measured by using microwave links [e.g., *Upton et al.*, 2007]. A radiation closure study at multiple frequencies has been proposed by *Bennartz and Kulie* [2012] to validate scattering models. However, both of these methods rely on knowing the physical properties of snowflakes, which is generally not possible without a controlled laboratory environment.

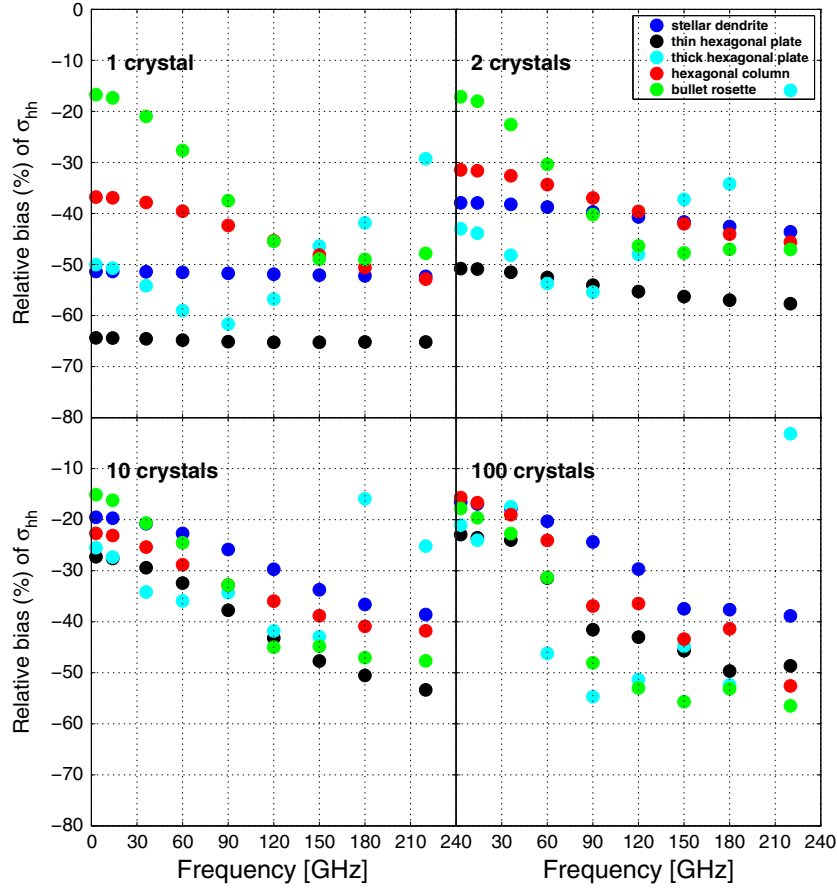


Figure 3. The average relative bias of the horizontal backscattering cross-section $100(\sigma_{\text{hh,RGA}} - \sigma_{\text{hh,DDA}})/\sigma_{\text{hh,DDA}}$ as a function of frequency.

3. Results

[24] In the present study, we have modeled physically realistic snowflakes of various shapes and sizes to compare their single-scattering properties obtained with the RGA and the DDA. The single-scattering properties have been computed at nine different frequencies between 3 and 220 GHz. The monomer types in the aggregates have been chosen to be distinct from each other. Extreme shapes are used to get a sufficiently diverse base for testing the performance of the RGA.

3.1. Mass-Diameter Relationship

[25] Figure 2 shows the mass of the modeled snowflakes as a function of their maximum diameter D_{max} in the horizontal plane. The empirical mass-diameter relations of the form $m = \alpha D_{\text{max}}^\beta$ are shown for snow by *Matrosov* [2007] and *Mitchell* [1996], and for corresponding single ice crystals by *Heymsfield* [1987], *Mitchell* [1990], and *Heymsfield* [1975], following the classification of *Magono and Lee* [1966]. As can be seen, the average mass of the snowflakes is close to the empirical curves for snow. There is some deviation from the empirical curves for single crystals, but these differences are mainly due to the fact that we wanted to use fixed and more extreme values for the aspect ratios in order to check the applicability of the RGA. In nature, the aspect ratios vary between shapes and are functions of D_{max} .

The almost constant mass for the 100-monomer aggregates (square symbols) is due to the fact that, when there are large number of crystals in an aggregate, the size variation of single crystals has less influence on the total mass. For single crystals, there is a clear mass-diameter relation for all crystal types. It is also clear that aggregates of dendrites are the fluffiest and aggregates of rosettes and thick plates the densest, with aggregates of columns and thin plates in the middle having similar densities. Notice that the measured curve for hexagonal plates (black line) lies between the thin (black dots) and thick plates (cyan dots).

3.2. Backscattering and Extinction Cross-Sections

[26] In Figures 3 and 4, we show the biases $(100(\sigma_{\text{RGA}} - \sigma_{\text{DDA}})/\sigma_{\text{DDA}})$ of the backscattering and extinction cross-sections for the RGA relative to the reference DDA computations as a function of frequency.

[27] For the horizontal cross-section σ_{h} (Figure 3), it is clear that the RGA is able to reproduce the DDA values for all shapes with a relative bias of at worst -65% . Compared to the order of a magnitude error for spheres reported in earlier studies (see section 1), this is a big improvement. The overall tendency is for the biases to become smaller with an increasing number of monomers in the aggregates and larger with increasing frequency of the incident wave. The monomer shape has more complex tendencies with respect to the number of monomers and frequency. For

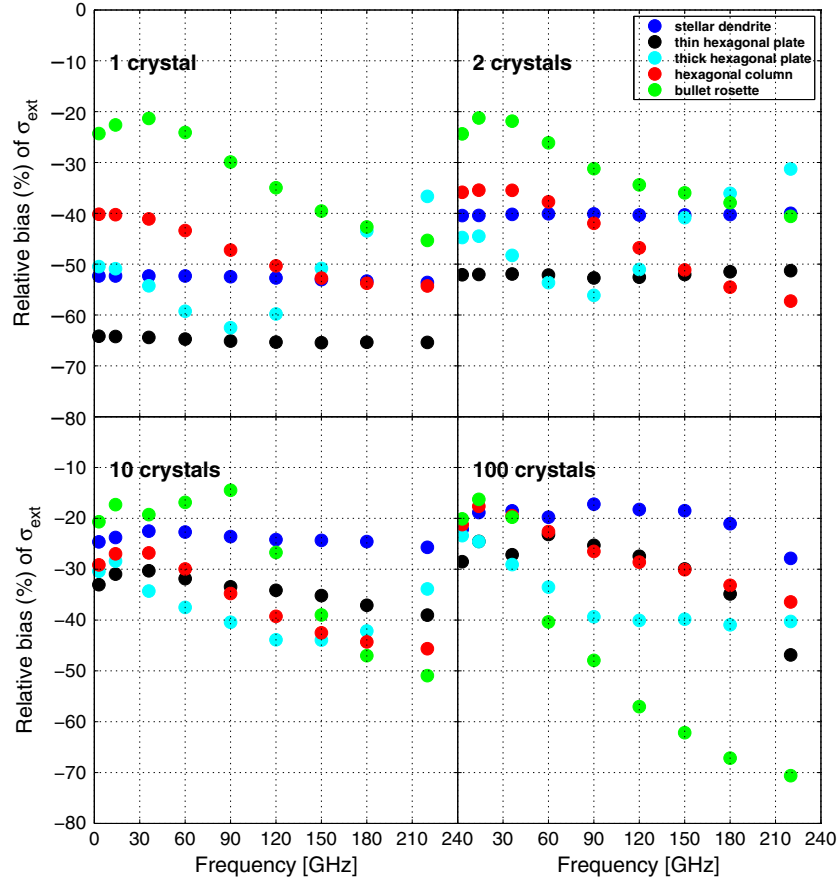


Figure 4. Same as in Figure 3, but for the extinction cross-section σ_{ext} .

single crystals, there is a clear separation in the bias between monomer shapes. Bullet rosettes are the most accurate with hexagonal columns being second accurate followed by stellar dendrites. The plates are the least accurate with the thick plates showing better accuracy at higher frequencies. Dendrites and plates have an almost constant bias regardless of the frequency. Two-monomer aggregates show a similar behavior, except for the dendrites and plates exhibiting more variation in the bias. For both 10- and 100-monomer aggregates (bottom row), the differences between monomer shapes are diminished, and the accuracy is only slightly better for the 100-monomer aggregates. For these larger aggregates, dendrites are the most accurate with columns being the second. Again, thin plates are overall the least accurate, but the accuracy of rosettes seems to decrease faster than for the other shapes as the size parameter increases. The thick plates show a large variation in accuracy being the most accurate at higher frequencies and least accurate at intermediate frequencies. There is a constant bias of about 20% regardless of the monomer shape for the larger aggregates.

[28] There are two main physical properties of snowflakes/ice crystals that control the accuracy of the RGA relative to the DDA: the aspect ratio and mass/density. Note that the single crystals are oriented horizontally because of their symmetric shapes; the principal axes are always aligned according to their major dimensions. At the backscattering angle, the form factor depends only on the relative positions of the volume elements in the incident direction. For flat crystals, such as dendrites and thin plates, it equals

unity regardless of the frequency. This explains the almost constant relative bias for these shapes. Also, at small size parameters, the form factor is close to unity, and the RGA is essentially the classical Rayleigh approximation for spheres, which is less accurate for elongated shapes in a fixed orientation. For the single-crystal columns and rosettes, this is clearly seen in the negative bias increasing monotonically as the size parameter increases. There is a constant shape-dependent bias for small size parameters that is mainly due to their different aspect ratios. This constant bias is also seen for the 10- and 100-monomer aggregates. It can be explained by their average aspect ratio of about 0.6. However, density is not the important property for the accuracy of single crystals, since rosettes and thick plates that are the densest of the crystals are also the most accurate. For the 100-monomer aggregates, the rosettes are the least accurate. This may be because, as they have the most massive monomers, the interactions between the volume elements become significant at smaller size parameters than for the other monomer shapes. On the other hand, the thick plates, which are equally massive, show an increase in accuracy at high frequencies.

[29] Even though σ_{ext} (Figure 4) is an integrated quantity and σ_{hh} is differential, they have overall the same accuracy with maximum negative biases of -70% . Somewhat surprisingly, σ_{ext} is also more strongly a function of the monomer shape. It should be noted that, for $\sigma_{\text{ext, RGA}}$, the form factor equals unity, meaning that $\sigma_{\text{ext, RGA}}$ is the same as obtained from the Rayleigh approximation for spheres.

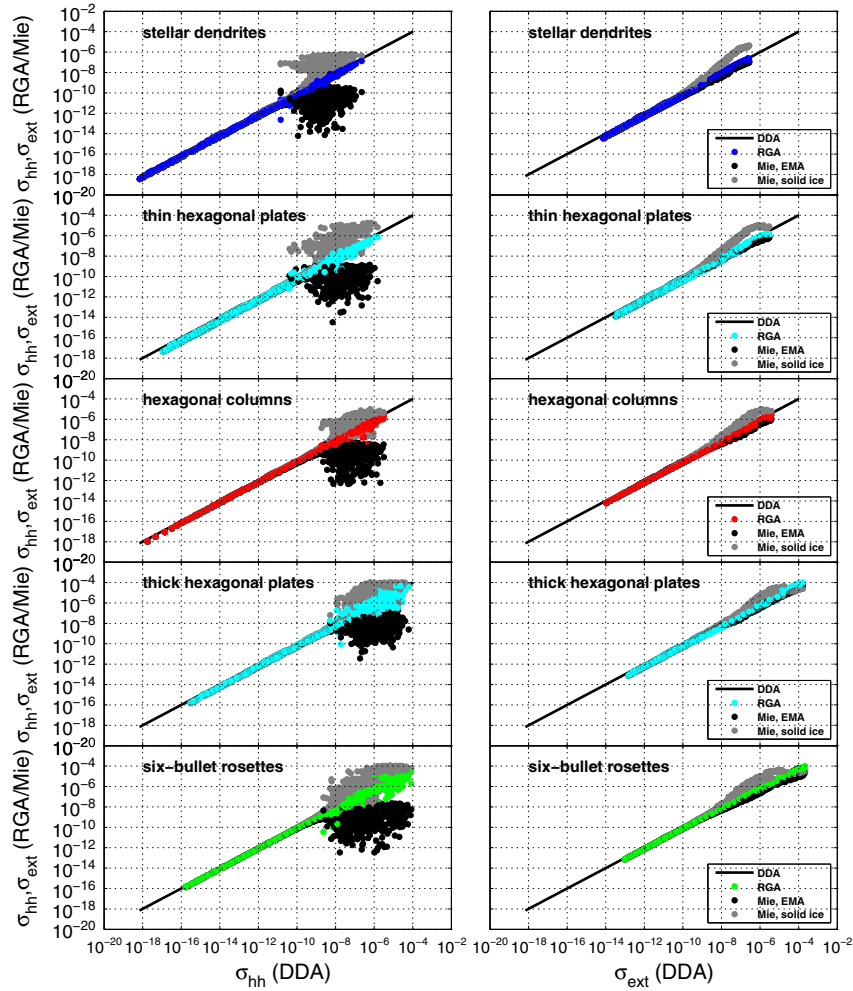


Figure 5. Scatter plots for the horizontal backscattering (left column) and extinction cross-sections (right column). The DDA results are on the X axis, while the RGA/Mie results are on the Y axis. The DDA results are plotted in black solid lines, the RGA in colored dots, the volume-equivalent Mie solutions in gray dots, and the effective-volume Mie solutions in black dots. Each color represents different types of crystal. Some symbols may be overlapping.

The tendencies between the number of monomers, frequency, and monomer shape are quite similar to those for σ_{hh} . Only the rosettes show clearly distinct differences by the fast decrease in accuracy as the size parameter increases. The thick plates are almost as inaccurate as the rosettes on average, but are more accurate at higher frequencies.

[30] There is also a localized minimum in bias at 14 GHz. The -20% constant relative bias at small size parameters that was found in σ_{hh} can also be seen in σ_{ext} . One particular difference between σ_{hh} and σ_{ext} is that the accuracy of plates and dendrites is almost unaffected by the frequencies used in this study. The explanations for the tendencies in σ_{ext} are the same as for σ_{hh} .

[31] Figure 5 shows the scatter plots for backscattering and extinction cross-sections. We also include computations using the Mie theory for both volume-equivalent and effective-volume cases. In the effective-volume cases, we use spheroids with equal maximum diameter and aspect ratio as the volume, and the MG EMA with ice as the inclusions to compute the effective refractive index.

[32] Overall, it is clear that the RGA has a linear dependence with the DDA for all shapes and frequencies. There is a threshold, between 10^{-11} and 10^{-8} m^2 depending on the crystal type, above which the variance in the cross-sections increases greatly. The corresponding volume-equivalent-sphere size parameters vary between 0.1 and 0.4 and maximum-diameter size parameters $kD_{max}/2$ between 0.5 and 1.1 at the threshold. Below the threshold, there is not much difference between crystal types. Above the threshold, the rosettes and thick plates show largest variance, while the dendrites show the lowest. The threshold is attributed to the resonance regime, where the interactions between the volume elements start to become significant. However, the mean values of cross-sections for RGA stay close to those for the DDA even above the threshold. This is because the assumption of the RGA that the volume elements do not interact strongly is generally true for realistically shaped snowflakes, while it is not true for the spherical particles.

[33] Above the threshold cross-section, the volume-equivalent spheres can overestimate the cross-sections by about a factor of 100 for σ_{hh} and about a factor of 10 for

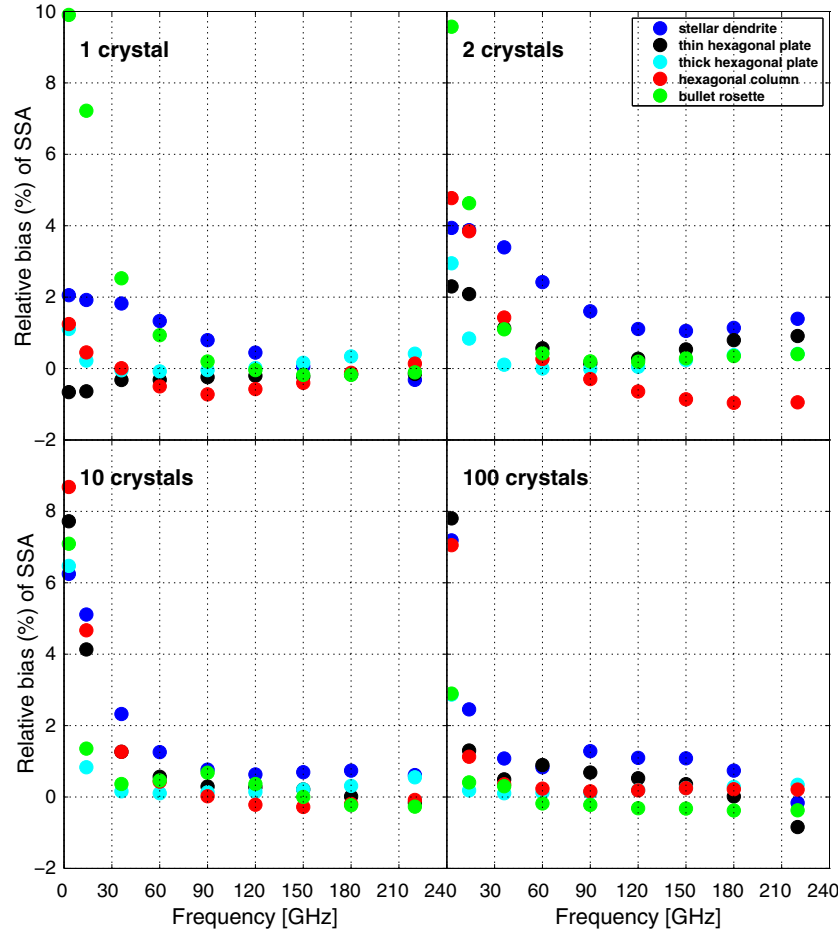


Figure 6. Same as in Figure 3, but for the single scattering albedo SSA.

σ_{ext} . There is not much difference between crystal types, but the stellar dendrites show clearly the largest differences between Mie and DDA results. At large cross-sections, the differences appear to become smaller. The effective-volume spheres on the other hand can underestimate σ_{hh} by a factor of 1000 and σ_{ext} by a factor of 5 on average. At the resonance regime, the volume elements interact strongly due to the symmetric shape. This interaction results in over/underestimation. For cross-sections below the threshold, any of the methods are equally suitable as compared to DDA.

3.3. Single-Scattering Albedo and Asymmetry Parameter

[34] In Figures 6 and 7, we show the biases of the single-scattering albedo and asymmetry parameter for the RGA relative to the reference DDA computations as a function of frequency.

[35] The single-scattering albedo ϖ (Figure 6) is the most accurate of the scattering quantities considered in this study with about 10% maximum positive bias against the DDA. As for the cross-sections, there is a tendency of the biases to get smaller as the number of monomers increases in aggregates, but unlike the cross-sections, the biases get smaller as the frequency increases. The differences between monomer shapes are not very significant, except at small size parameters for single crystals.

[36] As ϖ is the ratio of σ_{sca} and σ_{ext} , we also checked the accuracy of σ_{sca} and σ_{abs} (not shown). Both σ_{sca} and σ_{abs} have similar accuracies as σ_{hh} as a function of frequency, and similar tendencies between the number of monomers and monomer shapes.

[37] At small frequencies, there seems to be a varying bias for all shapes. At those size parameters, absorption dominates over scattering, and ϖ is small. Equation (4) indicates that $\sigma_{\text{abs},\text{RGA}}$ is not affected by the shape at all, but only by the volume, due to the optical theorem. The differences between shapes are therefore mainly due to the different volumes/masses. For the larger size parameters/frequencies, ϖ for all the shapes are very accurate with less than 2% relative bias with respect to the DDA. For larger size parameters, scattering starts to dominate over absorption, and ϖ is close to unity. Since it is the ratio of two similar cross-sections, the inaccuracies apparently cancel each other.

[38] The asymmetry parameter g (Figure 7) is shown in unnormalized scale due to the almost zero values of g_{DDA} . For all shapes and sizes, the bias stays below 0.12. Columns, plates, and dendrites have similar accuracy for all sizes and there does not seem to be systematic differences between them. Rosettes, on the other hand, are clearly the least accurate of the monomer shapes. They show an increasing positive bias with increasing size parameter for single crystals and two-monomer aggregates, but an increasing negative bias for 10- and 100-monomer

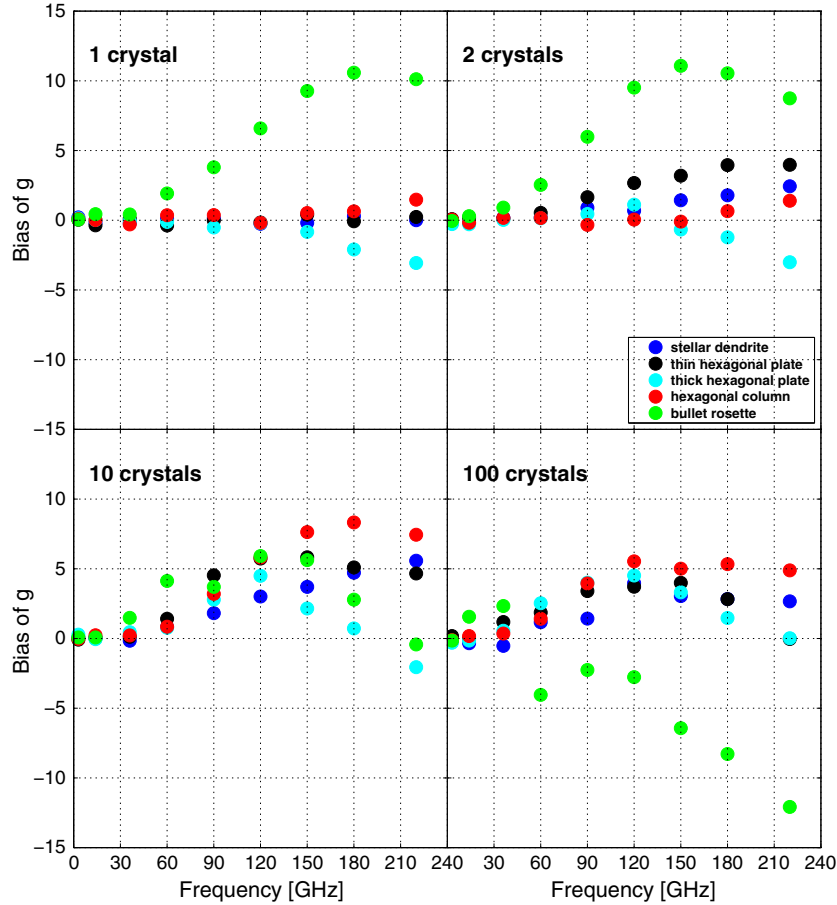


Figure 7. The average unnormalized bias of the asymmetry parameter $g_{\text{RGA}} - g_{\text{DDA}}$ as a function of frequency.

aggregates. A downward trend is also seen for the other shapes at 100-monomer aggregates, but generally the RGA overestimates g at these frequencies. The maximum in the bias occurs approximately at volume-equivalent-sphere size parameter $x = 1$ for all monomer shapes. To explain the presence of the maximum requires a more thorough study, but it is generally known that, when the particle sizes are comparable to the wavelength (resonance region), interactions between the volume elements start to become significant. The angular distribution of these interactions depends on the shape, refractive index, size parameter, and orientation of the particle, but averaging tends to make the angular distribution more isotropic. However, in the forward scattering direction, the interactions are always coherent. We speculate that due to this effect, the asymmetry parameter tends to increase more rapidly for the DDA than for the RGA, which does not include these interactions.

[39] Figure 8 shows the scatter plots for ϖ and g similar to Figure 5. As with the cross-sections, the RGA demonstrates great linear dependence also for ϖ and g with respect to the DDA results. The single-scattering albedo is clearly the most accurate of the scattering properties when using RGA and asymmetry parameter the least accurate. Even though there is a large variance from the DDA for g , on average the RGA is performing well. The largest variance of g occurs at intermediate values, which correspond to volume-equivalent-sphere size

parameters of 1.0–3.0 and maximum-diameter size parameters of 3–12.

[40] When using the Mie theory, the accuracy of ϖ is strongly dependent on the crystal type. Thicker crystals are more accurate with the Mie theory than the thin plate-like crystals. Again, the volume-equivalent spheres can overestimate ϖ by 0.1, while the effective-volume spheres can underestimate it by 0.05. The asymmetry parameter shows large variance for the Mie solutions when compared to the DDA. Overall, the volume-equivalent spheres can underestimate g by 0.5, while the effective-volume spheres can overestimate it by 0.4. In light of these results, estimating the asymmetry parameter for snowflakes at microwave frequencies using the Mie theory is highly questionable.

3.4. Empirical Corrections to RGA

[41] Since many of the errors in the RGA appear to take the form of a fractional bias which varies weakly as a function of the size parameter, we now derive a set of correction factors for the RGA-based quantities (q). In Tables 1–4, the correction factors α for the RGA are shown in the form: $q_{\text{DDA}} = \alpha q_{\text{RGA}}$ for each frequency. For a given monomer shape and frequency, all samples, sizes, and orientations are used in the fitting. A constant fitting term (bias) is close to zero for all the cases, so it is omitted. The corresponding sample correlation coefficients (r) are also shown in the

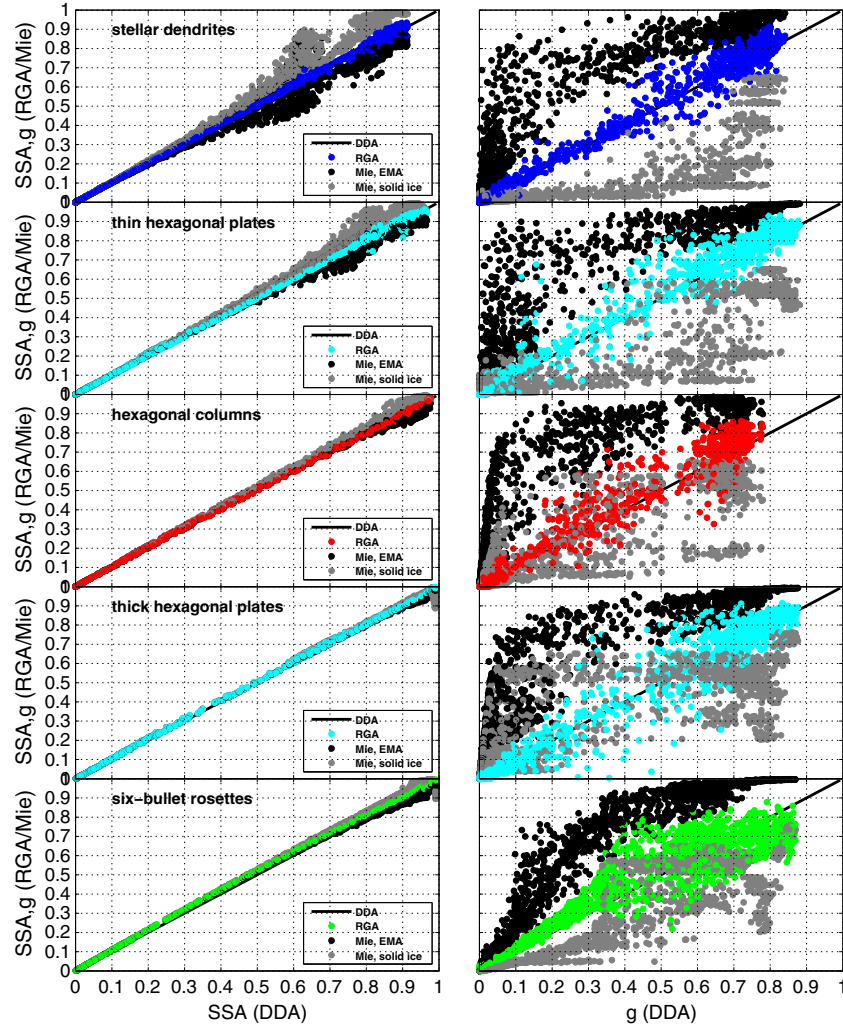


Figure 8. Same as in Figure 5, but for the single scattering albedo (left column) and asymmetry parameter (right column).

Table 1. Linear Fitting (α) and Correlation Coefficients (r) for the Horizontal Backscattering Cross-Sections Between the RGA and the DDA^a

Shape		Frequency (GHz)								
		3	14	36	60	90	120	150	180	220
Stellar dendrite	α	1.199	1.204	1.224	1.277	1.325	1.423	1.574	1.584	1.639
	r	0.999	0.999	0.998	0.993	0.989	0.984	0.989	0.992	0.989
Thin hexagonal plate	α	1.302	1.307	1.328	1.530	1.669	1.788	1.908	2.108	2.393
	r	0.998	0.998	0.990	0.976	0.987	0.982	0.982	0.983	0.966
Thick hexagonal plate	α	1.267	1.319	1.352	1.682	2.099	1.860	1.534	1.537	1.451
	r	0.999	0.998	0.970	0.932	0.838	0.747	0.659	0.671	0.669
Hexagonal column	α	1.185	1.201	1.251	1.364	1.480	1.495	1.605	1.579	1.692
	r	0.998	0.998	0.996	0.982	0.976	0.966	0.946	0.934	0.884
Six-bullet rosette	α	1.217	1.245	1.298	1.367	1.773	1.944	1.973	1.702	1.621
	r	1.000	1.000	0.996	0.987	0.945	0.862	0.819	0.717	0.596

^aThe values have been rounded up to three decimal places.

tables in order to check how linear the correlation between the RGA and the DDA is. Values of r that are close to unity mean a very good correlation.

[42] In Table 1, it is seen that $\sigma_{\text{hh,RGA}}$ is underestimated with respect to $\sigma_{\text{hh,DDA}}$. The correction factor generally increases as the frequency increases, and varies between 1.2

and 2.4 (0.8–3.8 dB) depending on the monomer shape and frequency. The correlation between the DDA and the RGA quantities is very good for all the shapes, showing only minor deviation for the bullet-rosette aggregates at high frequencies (>120 GHz). It is again clear that dendrites are the most accurate with columns being the close second. Thin

Table 2. Same as in Table 1, but for the Extinction Cross-Sections

Shape		Frequency (GHz)								
		3	14	36	60	90	120	150	180	220
Stellar dendrite	α	1.289	1.241	1.230	1.224	1.213	1.272	1.195	1.274	1.345
	r	1.000	1.000	0.998	0.988	0.977	0.978	0.977	0.980	0.969
Thin hexagonal plate	α	1.411	1.337	1.365	1.389	1.360	1.356	1.383	1.504	1.783
	r	1.000	1.000	0.994	0.987	0.983	0.978	0.976	0.972	0.972
Thick hexagonal plate	α	1.312	1.328	1.393	1.573	1.608	1.667	1.604	1.632	1.570
	r	1.000	0.999	0.989	0.980	0.966	0.968	0.965	0.962	0.968
Hexagonal column	α	1.275	1.225	1.274	1.344	1.499	1.511	1.684	1.450	1.635
	r	1.000	1.000	0.999	0.987	0.981	0.973	0.972	0.976	0.973
Six-bullet rosette	α	1.253	1.200	1.215	1.562	1.826	2.078	2.424	2.501	2.802
	r	1.000	0.999	0.986	0.967	0.972	0.960	0.970	0.963	0.943

plates are the least accurate with rosettes and thick plates in between.

[43] Dual-frequency ratios (DFR) between the backscattering cross-sections at Ku (14 GHz), Ka (36 GHz), and W (90 GHz) bands are used to distinguish different snow/ice crystal types [Matrosov, 1998; Hogan *et al.*, 2000; Kneifel *et al.*, 2011]. DFRs are computed by integrating over particle-size distributions. As we have shown, for a given frequency, the correction factors are similar for different sized snowflakes. We can therefore compute the DFRs using the correction factors for the averaged cross-sections. The correction factors for the $\text{DFR}_{\text{Ku/Ka}}$ are 1.017, 1.016, 1.025, 1.042, and 1.043 for the dendrites, thin plates, thick plates, columns, and rosettes, respectively. For $\text{DFR}_{\text{Ka/W}}$, the correction factors are 1.083, 1.257, 1.553, 1.183, and 1.366.

[44] Table 2 shows the correction factors for $\sigma_{\text{ext,RGA}}$. Again, there is an underestimation with respect to $\sigma_{\text{ext,DDA}}$ with the correction factor varying between 1.2 and 2.8, although the correlation is nevertheless better than for σ_{hh} . Dendrites are again the most accurate, while rosettes are the least accurate. Columns and plates have similar accuracies in between.

[45] The correction factors and correlations for ϖ are shown in Table 3. As can be seen, they are close to unity for most shapes and frequencies with a very good correlation throughout. The accuracy of ϖ is almost unaffected by the monomer shape.

[46] In Table 4, we show the correction factors for g , which is overestimated slightly by the RGA for all shapes. The correction factor varies between 0.6 and 1.0, but is overall close to unity. The correlation is worse for the large

Table 3. Same as in Table 1, but for the Single-Scattering Albedos

Shape		Frequency (GHz)								
		3	14	36	60	90	120	150	180	220
Stellar dendrite	α	0.935	0.975	0.982	0.984	0.988	0.989	0.990	0.992	0.994
	r	1.000	1.000	1.000	0.999	0.999	0.999	0.998	0.996	0.993
Thin hexagonal plate	α	0.929	0.987	0.990	0.993	0.995	0.996	0.997	0.999	1.002
	r	1.000	1.000	1.000	1.000	0.999	0.998	0.996	0.991	0.978
Thick hexagonal plate	α	0.971	0.994	0.998	0.999	0.999	0.999	0.999	0.998	0.997
	r	1.000	1.000	1.000	1.000	1.000	0.999	0.998	0.995	0.989
Hexagonal column	α	0.930	0.988	0.991	0.996	0.999	1.001	1.002	1.002	1.002
	r	1.000	1.000	1.000	1.000	1.000	0.999	0.999	0.999	0.998
Six-bullet rosette	α	0.971	0.986	0.992	0.995	0.996	0.998	0.999	1.000	1.000
	r	1.000	1.000	1.000	0.999	0.998	0.997	0.993	0.984	0.973

Table 4. Same as in Table 1, but for the Asymmetry Parameters

Shape		Frequency (GHz)								
		3	14	36	60	90	120	150	180	220
Stellar dendrite	α	-	0.608	0.992	0.957	0.964	0.944	0.952	0.949	0.944
	r	-	0.736	0.989	0.993	0.992	0.989	0.990	0.988	0.985
Thin hexagonal plate	α	-	0.907	0.972	0.964	0.933	0.943	0.941	0.954	0.978
	r	-	0.920	0.994	0.994	0.993	0.990	0.986	0.980	0.966
Thick hexagonal plate	α	-	0.8841	0.9726	0.963	0.936	0.945	0.944	0.954	0.979
	r	-	0.922	0.994	0.994	0.993	0.990	0.987	0.980	0.967
Hexagonal column	α	-	0.556	0.958	0.962	0.921	0.894	0.911	0.885	0.892
	r	-	0.703	0.987	0.995	0.992	0.986	0.974	0.965	0.967
Six-bullet rosette	α	-	0.893	0.977	0.942	0.954	0.944	0.950	0.964	0.987
	r	-	0.979	0.988	0.974	0.974	0.954	0.895	0.831	0.769

bullet-rosette aggregates. At 3 GHz, we were unable to fit the data due to small, negative values.

4. Discussion

[47] The results of section 3 indicate that the Rayleigh-Gans approximation is a reasonably accurate and predictable method for computing scattering by aggregate snowflakes at microwave frequencies. The minimum relative bias of -60% in the backscattering cross-section σ_{hh} corresponds to a bias of -4 dB compared to the results computed with the DDA, while the more typical bias of -40% equals roughly -2 dB. Similar biases are found for the extinction cross-section σ_{ext} . These are the most important quantities for radar studies, σ_{hh} specifying the reflectivity and σ_{ext} the attenuation of the radar signal. The bias of both σ_{hh} and σ_{ext} is quite stable, and thus the correction factors given in Tables 1 and 2 can be used to reduce the bias. The expected remaining bias of 1 – 2 dB is only slightly higher than a typical radar measurement error. The single-scattering albedo and the asymmetry parameter, relevant for radiometric studies (and also for radars in the presence of multiple scattering between snowflakes), have much smaller biases and thus are not expected to introduce significant additional errors.

[48] These findings are consistent with the previous success with the theoretical and modeling studies by *Westbrook* [2006]. In contrast, despite the relatively comprehensive data set we used, our results do not reproduce the much greater (up to 7 dB) discrepancies in the backscattering cross-section reported by *Petty and Huang* [2010]. Their monomers and the aggregate generation algorithm appear to be quite similar to ours, but their results are for individual snowflakes whereas we averaged over several snowflakes. Although the variance for the RGA increases greatly at the resonance region (Figures 5 and 8), they tend to average out as shown in Figures 3, 4, 6, and 7. Therefore, we suggest that the comparatively high bias obtained by *Petty and Huang* [2010] was due to a coincidental selection of snowflakes with unusually large differences between the RGA and DDA backscattering cross-sections, and therefore are not representative.

[49] The relatively good accuracy of the RGA compared to the DDA allows us to draw a number of interesting conclusions. Most obviously, it implies that the microwave scattering properties of snowflakes can be approximated well using a method that is computationally much faster than the DDA and is overall more accurate than the classical Rayleigh and Mie solutions. One special case where the RGA is not applicable is in computing polarimetric radar quantities, because the form of the amplitude scattering matrix for the RGA equals that for the Rayleigh approximation. For this purpose, a simple modification to the classical RGA was presented by *Hogan et al.* [2012].

[50] Perhaps more important than computational performance is the fact that the RGA is also mathematically very simple: the scattering matrix is obtained through scalar integration over the particle rather than by solving a vector integral equation. This greatly simplifies the analysis of the connection between the particle structure and scattering and allows for the application of previously developed techniques that use the RGA to analyze scattering from aggregates [*Sorensen*, 2001].

[51] It is also noteworthy that the discrepancy between the DDA and RGA computations of aggregates is much smaller than the difference sometimes seen between aggregates and the equivalent spheres or spheroids (Figures 5 and 8). Hence, we conjecture that particle morphology, particularly the inhomogeneity of snowflakes, is the major contributor to the difference between spheroid models and real snowflakes, with the details of the interactions in the particle playing a relatively minor role.

[52] One hypothesis is that, as the larger aggregates are less dense than the smaller ones, they satisfy the RGA requirements of equation (11) better. However, it is not immediately evident what would the size parameter and the refractive index be for irregular particles. In the present study, we show that the RGA is applicable to irregular shapes, such as snowflakes, at microwave region of the electromagnetic spectrum. However, in equation (9), we use the volume and refractive index of solid ice. Using these in equation (11) will not satisfy the classical requirements. It is usually assumed that replacing an irregular particle with one that has the same effective volume and aspect ratio is justified even at the resonance region. Indeed, it can be shown that the assumption of noninteractive volume elements in equation (9) is equal to using the Maxwell Garnett formula with ice as the inclusions and air as the matrix. However, the effect of irregular shape and inhomogeneity on the scattering properties, represented by the form factor in the RGA, cannot be mimicked with choosing an appropriate density and/or aspect ratio.

[53] We investigated this by computing effective refractive indices using the Maxwell Garnett formula. In order to estimate the volume fractions of the particles, spheroids with the same average D_{max} and aspect ratio were used as the volumes. With the exception of single crystals, both the RGA requirements of equation (11) were fulfilled reasonably well on average. However, based on our investigation, it is still unclear whether equation (11) can be used to validate the RGA for fluffy particles mainly because of the ambivalence of choosing how to define x and m .

5. Conclusion

[54] We have computed single-scattering properties of realistic snowflakes using both the DDA and the RGA and covering a wide range of microwave frequencies. We have used common monomer shapes in the snowflakes: stellar dendrites, thin and thick hexagonal plates, hexagonal columns, and six-bullet rosettes. The number of monomers in the snowflakes is also varied.

[55] The main conclusion is that the RGA and the DDA agree within a factor of about two or better for all the single-scattering properties investigated in the present study. Compared to the orders of magnitude differences in the backscattering cross-sections between realistic shapes and spheroid models reported by previous studies (see section 1) and also shown in this study, it is a significant improvement. Also, the linear relation between the scattering characteristics of the DDA and the RGA indicates that the correction factors can be used consistently regardless of the radar/radiometer frequency.

[56] For the RGA backscattering and extinction cross-sections, there is about -65% relative underestimation for

small aggregates and $\sim 50\%$ for large aggregates. Rosettes show larger variance by being most accurate of the monomer shapes for small aggregates and least accurate for large aggregates. There is a $\sim 20\%$ constant bias for all shapes, which is due to the aspect ratio and the preferential orientation of the aggregates. Overall, the correlation coefficients are close to unity for both the backscattering and extinction cross-sections.

[57] The integrated scattering quantities, such as the single-scattering albedo and the asymmetry parameter, are more accurate compared to the backscattering and extinction cross-sections. The single-scattering albedo is the most accurate of the quantities, with the correction factors and sample correlation coefficients close to unity for all shapes and frequencies. The asymmetry parameter is also very accurate, only showing deviations for the rosettes at high frequencies. The RGA slightly overestimates both the single-scattering albedo and the asymmetry parameter. This indicates that the RGA is better for radiative transfer computations than for single-scattering studies.

[58] **Acknowledgments.** The authors would like to thank Evgenij Zubko for his comments. We also want to thank the Finnish Center for Scientific Computing (CSC) for providing the computational resources to do the study. This work was supported by the Academy of Finland (contracts 125180, 128255, and 128328).

References

- Austin, R. T., A. J. Heymsfield, and G. L. Stephens (2009), Retrieval of ice cloud microphysical parameters using the CloudSat millimeter-wave radar and temperature, *J. Geophys. Res.*, **114**, D00A23, doi:10.1029/2008JD010049.
- Bennartz, R., and M. Kulie (2012), Evaluating microwave ice particle scattering models using multi-frequency radiative closure studies, *Proc. Int. Radiation Symp 2012*, Berlin, Germany.
- Berry, M., and I. Percival (1986), Optics of fractal clusters such as smoke, *Opt. Acta*, **33**, 577–591, doi:10.1080/713821987.
- Bohren, C. F., and L. J. Battan (1980), Radar backscattering by inhomogeneous precipitating particles, *J. Atmos. Sci.*, **37**, 1821–1827, doi:10.1175/1520-0469(1980)037<1821:RBBIPP>2.0.CO;2.
- Bohren, C. F., and D. R. Huffman (1983), *Absorption and scattering of light by small particles*, 61–68, Wiley, New York.
- Botta, G., K. Aydin, and J. Verlinde (2010), Modeling of microwave scattering from cloud ice crystal aggregates and melting aggregates: A new approach, *IEEE Geosci. Rem. Sens. Lett.*, **7**, 572–576, doi:10.1109/LGRS.2010.2041633.
- Heymsfield, A. J. (1975), Cirrus uncinus generating cells and the evolution of cirriform Clouds. Part III: Numerical computations of the growth of the ice phase, *J. Atmos. Sci.*, **32**, 820–830, doi:10.1175/1520-0469(1975)032<0809:CUGCAT>2.0.CO;2.
- Heymsfield, A. J., and M. Kajikawa (1987), An improved approach to calculating terminal velocities of plate-like crystals and graupel, *J. Atmos. Sci.*, **44**, 1088–1099, doi:10.1175/1520-0469(1987)044<1088:AIATCT>2.0.CO;2.
- Hogan, R., A. Illingworth, and H. Sauvageot (2000), Measuring crystal size in cirrus using 35- and 94-GHz radars, *J. Atmos. Oceanic Technol.*, **17**, 27–37, doi:10.1175/1520-0426(2000)017<0027:MCSICU>2.0.CO;2.
- Hogan, R., and A. Battaglia (2008), Fast lidar and radar multiple-scattering models: Part II: Wide-angle scattering using the time-dependent two-stream approximation, *J. Atmos. Sci.*, **65**, 3636–3651, doi:10.1175/2008JAS2642.1.
- Hogan, R. J., L. Tian, P. R. A. Brown, C. D. Westbrook, A. J. Heymsfield, and J. D. Eastment (2012), Radar scattering from ice aggregates using the horizontally aligned oblate spheroid approximation, *J. Appl. Meteor. Clim.*, **51**, 655–671, doi:10.1175/JAMC-D-11-074.1.
- Hong, G., P. Yang, B. A. Baum, A. J. Heymsfield, F. Weng, Q. Liu, G. Heygster, and S. A. Buehler (2009), Scattering database in the millimeter and submillimeter wave range of 100–1000 GHz for nonspherical ice particles, *J. Geophys. Res.*, **114**, D06201, doi:10.1029/2008JD010451.
- Ishimoto, H. (2008), Radar backscattering computations for fractal-shaped snowflakes, *J. Meteor. Soc. Japan*, **86**, 459–469, doi:10.2151/jmsj.86.459.
- Jiang, J. H., and D. L. Wu (2004), Ice and water permittivities for millimeter and sub-millimeter remote sensing applications, *Atmos. Sci. Lett.*, **5**, 146–151, doi:10.1002/asl.77.
- Kneifel, S., M. Kulie, and R. Bennartz (2011), A triple frequency approach to retrieve microphysical snowfall parameters, *J. Geophys. Res.*, **116**, D11203, doi:10.1029/2010JD015430.
- Korolev, A., and I. G. Isaac (2003), Roundness and aspect ratio of particles in ice clouds, *J. Atmos. Sci.*, **60**, 1795–1808, doi:10.1175/1520-0469(2003)060<1795:RAAROP>2.0.CO;2.
- Liu, G. (2008), A database of microwave single-scattering properties for nonspherical ice particles, *Bull. Amer. Meteor. Soc.*, **89**, 1563–1570, doi:10.1175/2008BAMS2486.1.
- Magono, C., and C. W. Lee (1966), Meteorological classification of natural snow crystals, *J. Fac. Sci., Hokkaido Univ., Series VII*, **2**(4), 321–362.
- Matrosov, S. Y. (1992), Radar reflectivity in snowfall, *IEEE Trans. Geosci. Remote Sens.*, **30**, 454–461, doi:10.1109/36.142923.
- Matrosov, S. Y. (1998), A dual-wavelength radar method to measure snowfall rate, *J. Appl. Meteor.*, **37**, 1510–1521, doi:10.1175/1520-0450(1998)037<1510:ADWRMT>2.0.CO;2.
- Matrosov, S. Y. (2007), Modeling backscatter properties of snowfall at millimeter wavelengths, *J. Atmos. Sci.*, **64**, 1727–1736, doi:10.1175/JAS3904.1.
- Mie, G. (1908), Beiträge zur Optik trüber Medien, speziell kolloidaler Metallösungen, *Ann. Phys.*, **330**, 377–445.
- Mitchell, D. L., R. Zhang, and R. L. Pitter (1990), The mass-dimensional relationships for ice crystals and the influence of riming on snowfall rates, *J. Appl. Meteor.*, **29**, 153–163, doi:10.1175/1520-0450(1990)029<0153:MDRFIP>2.0.CO;2.
- Mitchell, D. L. (1991), Evolution of snow-size spectra in cyclonic storms. Part II: Deviations from the exponential form, *J. Atmos. Sci.*, **48**, 1885–189, doi:10.1175/1520-0469(1991)048<1885:EOSSSI>2.0.CO;2.
- Mitchell, D. L. (1996), Use of mass- and area-dimensional power laws for determining precipitation particle terminal velocities, *J. Atmos. Sci.*, **53**, 1710–1723, doi:10.1175/1520-0469(1996)053<1710:UOMAAD>2.0.CO;2.
- Penttilä, A., E. Zubko, K. Lumme, K. Muinonen, M. A. Yurkin, B. Draine, J. Rahola, A. G. Hoekstra, and Y. Shkuratov (2007), Comparison between discrete-dipole implementations and exact techniques, *JQSRT*, **106**, 417–436, doi:10.1016/j.jqsrt.2007.01.026.
- Petty, G. W., and W. Huang (2010), Microwave backscatter and extinction by soft ice spheres and complex snow aggregates, *J. Atmos. Sci.*, **67**, 769–787, doi:10.1175/2009JAS3146.1.
- Purcell, E. M., and C. R. Pennypacker (1973), Scattering and absorption of light by non-spherical dielectric grains, *Astrophys. J.*, **186**, 705–714, doi:10.1086/152538.
- Pruppacher, H. R., and J. D. Klett (1997), *Microphysics of Clouds and Precipitation*, pp. 58–63, Chap. 2, Springer, Dordrecht.
- Reiter, C. A. (2005), A local cellular model for snow crystal growth, *Chaos, Solitons and Fractals*, **23**, 1111–1119, doi:10.1016/j.chaos.2004.06.071.
- Sorensen, C. M. (2001), Light scattering by fractal aggregates: A review, *Aerosol Sci. Technol.*, **35**, 648–687, doi:10.1080/02786820117868.
- Takahashi, T., T. Endoh, and G. Wakahama (1991), Vapor diffusional growth of free-falling snow crystals, *J. Meteor. Soc. Japan*, **69**(1), 15–30.
- Tynnelä, J., J. Leinonen, D. Moisseev, and T. Nousiainen (2011), Radar backscattering from snowflakes: Comparison of fractal, aggregate and soft-spheroid models, *J. Atmos. Oceanic Technol.*, **28**, 1365–1372, doi:10.1175/JTECH-D-11-00004.1.
- Um, J., and G. M. McFarquhar (2007), Single-scattering properties of aggregates of bullet rosettes in cirrus, *J. Appl. Meteor. Clim.*, **46**, 757–775, doi:10.1175/JAM2501.1.
- Upton, G. J. G., R. J. Cummings, and A. R. Holt (2007), Identification of melting snow using data from dual-frequency microwave links, *IET Microw. Antennas Propag.*, **1**, 282–288, doi:10.1049/iet-map:20050285.
- Vaillon, R., J.-M. Geffrin, C. Eyraud, O. Merchiers, P. Sabouroux, and B. Lacroix (2011), A new implementation of a microwave analog to light scattering measurement device, *JQSRT*, **112**, 1753–1760, doi:10.1016/j.jqsrt.2010.12.008.
- van de Hulst, H. C. (1957), *Light scattering by small particles*, pp. 64–66, Wiley, New York.
- Waterman, P. C. (1965), Matrix formulation of electromagnetic scattering, *Proc. IEEE*, **53**, 805–812, doi:10.1109/PROC.1965.4058.
- Westbrook, C. D. (2004), Universality in snow formation, PhD thesis, University of Warwick, Coventry, UK.

- Westbrook, C. D., R. C. Ball, and P. R. Field (2006), Radar scattering by aggregate snowflakes, *Q. J. R. Meteorol. Soc.*, *132*, 897–914, doi:10.1256/qj.05.82.
- Wriedt, T., and U. Comberg (1998), Comparison of computational scattering methods, *JQSRT*, *60*, 411–423, doi:10.1016/S0022-4073(98)00016-8.
- Yurkin, M. A., M. Min, and A. G. Hoekstra (2010), Application of the discrete-dipole approximation to very large refractive indices: Filtered coupled dipoles revived, *Phys. Rev. E*, *82*, 036703, doi:10.1103/PhysRevE.82.036703.
- Yurkin, M. A., and A. G. Hoekstra (2011), The discrete-dipole-approximation code ADDA: Capabilities and known limitations, *JQSRT*, *112*, 2234–2247, doi:10.1016/j.jqsrt.2011.01.031.